Epitaxial growth of maghemite (001) and (111) on platinum: An ab-initio study

Amit Sahu, Julien Parize, Céline Dupont

Graphical Abstract

Epitaxial growth of maghemite (001) and (111) on platinum: an ab-initio study

Amit Sahu, Julien Parize, Céline Dupont

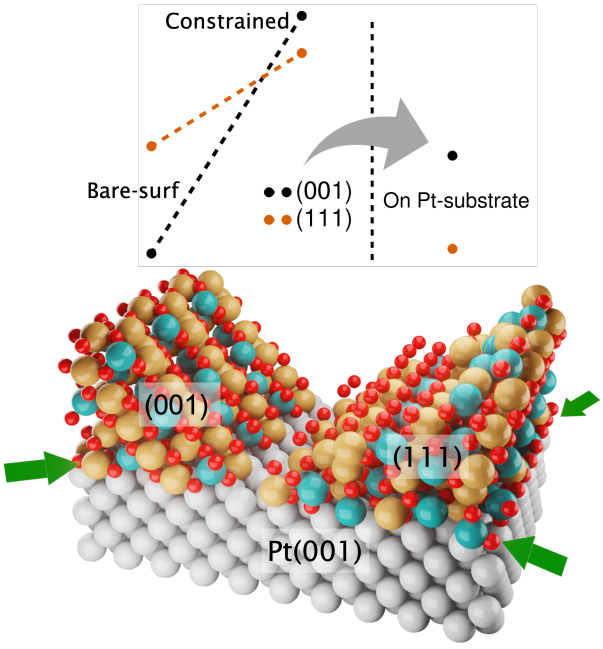

Highlights

Epitaxial growth of maghemite (001) and (111) on platinum: an ab-initio study

Amit Sahu, Julien Parize, Céline Dupont

- Maghemite (001) and (111) terminations modeled by density functional theory
- Strain and platinum substrate influences on energetic and electronic properties
- Isolated (001) favored over (111) termination
- (111) termination significantly favored when grown on platinum

Epitaxial growth of maghemite (001) and (111) on platinum: an ab-initio study

Amit Sahu[a], Julien Parize[a], Céline Dupont[a]

[a]*Laboratoire Interdisciplinaire Carnot de Bourgogne (ICB), UMR 6303 CNRS, Université Bourgogne Franche-Comté,, BP 47870, Dijon Cedex, 21078, France*

Abstract

In this study, maghemite, the second most stable iron oxide, has been investigated using a DFT+U approach. The relative stability of the different surface terminations from the (001) and (111) planes are discussed, allowing the discrimination of preferred terminations among oxygen vs. iron, with octahedral or tetrahedral cations sites, etc. To move towards epitaxial growth of maghemite on a Pt substrate, the strain effect induced by lattice mismatch is then considered, first for isolated maghemite, then when grown on the substrate. Among bare surfaces, (001) terminations are more stable than (111) ones, strain effect significantly destabilizes (001) in contrast with (111), resulting in a change in stability. Moreover, the lower formation energy indicates that the growth of the (111) surface will be favored over the one of the (001) on the Pt substrate due to numerous Pt-O interactions. Finally, various electronic properties such as bond-lengths, bonding, charges, and density of states are analyzed to understand the nature and stability of the surfaces. For surfaces, bandgaps are smaller than bulk, with a higher deviation for (001) than for (111) surfaces.

Keywords: maghemite, epitaxial growth, surface terminations, formation energies, density functional theory

1. Introduction

Nowadays, transition metal oxides are essential components for the development of novel catalysts for photoelectrochemical (PEC) water splitting because of their stability and abundance in nature. Particularly, iron-oxides have gained significant attention as they are readily synthesizable, have desired magnetic properties, and high electrical resistivity, and they are resistant to corrosion and aging[1, 2]. Their potential uses range from catalysis, magnetic drug delivery[3, 4, 5, 6], fuel cell[7, 8], and pollutant remover[9, 10, 11].

Maghemite surfaces have shown promising reactivity for oxygen evolution reaction, oxygen reduction reaction, photoelectrochemical water splitting[7, 12, 13, 14, 15], and CO oxidation.[16] Moreover, they are also proposed to be a cathode or anode material for Li-ion batteries[17]. A recent study shows an improvement on photo-catalytic activity of nanocomposite of reduced graphene oxide (RGO-$\gamma-Fe_2O_3$) over bulk $\gamma-Fe_2O_3$. [17] A phase junction of $\alpha-Fe_2O_3$ and $\gamma-Fe_2O_3$ offers a well separated charge carriers and reduced recombination rate[18] and helps to increase the catalytic activity.

Maghemite ($\gamma-Fe_2O_3$) is the second most stable polymorph among iron oxide phases. It presents a spinel structure derived from magnetite, and is ferrimagnetic in nature[2]. The unit cell is composed of tetrahedral and octahedral iron atoms, oxygen atoms, and vacancies at octahedral sites[19, 20]. When used as cathode, these iron vacancies facilitate the lithium intercalation thus allowing high capacity[21]. Low cost, exceptional stability in water even at high pH[22], natural abundance, and most importantly, a favorable band gap ($\sim$2.2 eV) in the visible light spectrum make it a promising candidate for photoanode in PEC water splitting. However, the high charge recombination rate and low conductivity are still significant constraints for efficient PEC water splitting. Various solutions can be deployed to overcome these hurdles such as control of morphology to increase charge-hole separation, nano-structuring, elemental doping, and the formation of heterostructures to refine the charge-transport properties[23, 24].

In all the uses of maghemite, the nature of species/sites present on surfaces is a decisive component to determine reactivity. Therefore, a reliable surface structure description is mandatory to understand the structure-reactivity relationship. A few efforts have been made to understand the surface structure

of $\gamma-Fe_2O_3$ to unveil the stability and reactivity. Baetzold and Yang performed two-dimensional periodic calculations along with mean-field approximation to gain insights into surface stability for various low-index surfaces containing the largest interplanar spacing. In absence of reconstruction, various low-index surfaces were found to be polar and unstable. Various surfaces showed similar surface energy within the range of 0.1 J/m^2. Moreover, (111) surface terminated with Fe_{Oh} has the lowest attraction energy. [25] The study of surface dependent adsorption properties on nanostructured particles using X-ray diffraction and IR spectroscopy[26] suggests a slight change in lattice parameter due to water adsorption depending on the water pressure and a number of water layers adsorbed on the surface. X-ray total scattering indicates a strong relaxation on smallest size nanoparticles.[27] Chambers and Joyce demonstrated γ-Fe_2O_3 (001) as (1×1) and that it is prone to chemisorb oxygen or hydroxyl groups by using surface sensitive electron diffraction and angle resolved X-ray photoemission.[28] However, another study suggests that reconstruction takes place on (001) surface and transforms it into $(\sqrt{2}\times\sqrt{2})$R45°.[29, 30, 31] A classical Monte-Carlo study was carried out to understand the surface effects of maghemite nanoparticles.[32] Reducing the particle size increases surface disorder and surface presents higher magnetic disorder than the core. Mou *et. al* synthesized rod-shaped nano-particles of $\gamma-Fe_2O_3$ with a diameter of 40 nm and length of 400 nm with a dominating end-plane of (110) and $(1\bar{1}0)$ and (001) as side planes[33]. Another study indicates the lower stability of Fe-tetrahedral atoms on the surface due to insufficient metal coordination with the ligands[21]. Low energy electron diffraction (LEED), X-ray photoelectron spectroscopy (XPS), ion-scattering spectroscopy (ISS), and scanning tunneling microscopy (STM) suggest the presence of two types of terminations for the (111) facet, namely the (2×2) and the $(\sqrt{3}\times\sqrt{3})$R30° reconstructions[34]. Furthermore, the role of oxygen vacancies for water oxidation and other reactions has been investigated by Jian[35] and Wang[15].

Unlike hematite[36, 37, 38, 39, 40, 41], maghemite has been inadequately understood due to competing claims among various models and random distribution of vacancies. Despite several attempts, the accurate understanding of maghemite surface terminations and their morphology is still incomplete. Moreover, maghemite is barely used alone but rather deposited on a substrate[42, 43, 44]. It thus appears essential to study the strain and electronic effects induced by this substrate during maghemite growth.

Given the reactivity of the (001) surface evidenced by Chambers *et al.*[28]

and the work of Baetzold *et al.*[25] which demonstrates that the (111) termination presents the lowest attachment energy, we decided to investigate these two terminations of $\gamma-Fe_2O_3$. Their equilibrium geometries, energetics, and electronic properties are thus compared. Besides this study of bare surfaces, the effect of strain due to the lattice mismatch with the substrate, here Pt(001), is considered and finally, we investigate the whole $\gamma-Fe_2O_3$/Pt(001) system. For each step, behaviors of (111) and (001) surfaces are compared.

2. Methods

2.1. Computational details

Calculations based on plane-wave density functional theory (DFT) have been carried out using the Vienna ab-initio simulation package (VASP 5.4.4)[45, 46]. Due to maghemite's ferrimagnetic nature, spin-polarised calculations are performed. To describe the interaction between iron-oxygen ions projector-augmented plane-wave (PAW) method is deployed[47]. Eight valence electrons for Fe ($3d^7 4s^1$), six for O ($2s^2 2p^4$), and ten for Pt ($5d^9 6s^1$) are treated explicitly in the PAW method. Perdew, Burke, and Ernzerhof (PBE) exchange-correlation functional approach is used within the general gradient approximation (GGA) framework[48]. Grimme D3 (DFT-D3) dispersion correction with zero damping is applied to account for long-range interactions[49]. Hybridization between *d*-orbitals of Fe and *p*-orbitals of O is significant due to the strongly correlated nature of maghemite. Over delocalization of *d*-electrons of Fe atoms within the DFT framework results in underestimation of the bandgap. This so called "bandgap" problem can be addressed using semiempirically tuned numerical parameter (U) which takes into account the localization of electrons within the same atomic orbital. We have used the DFT+U Dudarev approach[50] to localize the Fe-*d* electrons. A value of 4.3 eV for U_{eff} has been adopted, allowing a good agreement with experimental bulk properties [51, 52]

The Brillouin zone sampling is done by Monkhorst-Pack k-point mesh of 8×8×1 for (001) as the cell size is 8.39Å×8.39Å×32Å, but only Γ point is used for (111) surface due to the much larger supercell (19.60Å×11.76Å×49 Å). To enhance the convergence and minimize the electronic energy, Gaussian smearing with a smearing width of 0.1 is used while using a mixture of the blocked-Davidson scheme and residual minimization method. The kinetic energy cutoff is set to be 550 eV and the convergence threshold for energy and forces are set to 10^{-6} eV and 0.01 eV/Å respectively. For the bare

maghemite surface, all atoms are allowed to relax. However, for composite of maghemite/Pt(001), the bottom two layers of Pt substrate are kept fixed. A slab model truncated from bulk is used to describe all surface terminations, and a large vacuum of 20 Å is used to avoid the spurious interactions with periodic images along the z-direction. Finally, the convergence of 18-Layers slab model is relatively tricky. Therefore, we have first run a single point calculation with tight convergence criteria and enforcing the parameter `AMIX = 0.8, BMIX = 0.9, AMIX_MAG = 0.4, and BMIX_MAG = 0.9`, to make sure the right magnetic alignment for Fe species is obtained. Thereafter, we use the previously generated charge density (CHGCAR) and wavefunction (WAVECAR) to relax the structure and find the ground state minima.

2.2. Surface and interaction energies

In the following, we define the cleavage energy as the energy required to cut the bulk and thus create a slab with two surfaces. The cleavage energy per surface unit is calculated by using the following equation:

$$\gamma_{cleav} = \frac{1}{S} \times (E_{slab} - m \times E_{bulk}) \tag{1}$$

where E_{slab} and E_{bulk} are the energies of the slab and bulk structures, respectively, while m corresponds to the number of bulk units in the slab and S to the area of the slab unit cell.
The cleavage energy can also be defined in terms of surface energy (γ_S), with $\gamma_{cleav} = 2 \times \gamma_S$ for symmetric slabs and $\gamma_{cleav} = \gamma_{S1} + \gamma_{S2}$ for non-symmetric ones.

To quantify the impact of strain we define the strain energy per surface unit as follows:

$$\Delta E_{strain} = \frac{E^{strained}_{\gamma-Fe_2O_3} - E^{unstrained}_{\gamma-Fe_2O_3}}{S^{strained}}, \tag{2}$$

where $E^{unstrained}_{\gamma-Fe_2O_3}$ and $E^{strained}_{\gamma-Fe_2O_3}$ are the total energy of maghemite slab, native and strained, respectively, and $S^{strained}$ is the area of the strained unit cell. In order to understand the strength of the interaction between Pt(001) and strained maghemite we compute the interaction energy per surface unit with the following equation[41]:

$$\Delta E_{int} = \frac{E_{\gamma-Fe_2O_3/Pt} - E^{strained}_{\gamma-Fe_2O_3} - E_{Pt}}{S^{strained}} \tag{3}$$

where $E_{\gamma-Fe_2O_3/Pt}$ is the total energy of the whole system, $E^{strained}_{\gamma-Fe_2O_3}$ is the total energy of strained maghemite surface and E_{Pt} is the total energy of the Pt(001) substrate. To comprehend the stability of the different heterostructures, we evaluate the required formation energy (per surface unit) to generate the surface from its bulk on the Pt substrate. The following definition is used:

$$E_{formation} = \frac{E_{\gamma-Fe_2O_3/Pt} - E_{Pt} - E^{bulk}_{\gamma-Fe_2O_3}}{S^{strained}} \tag{4}$$

In the following, we will also discuss the adhesion energy defined as the sum of strain energy and interaction energy, namely:

$$\Delta E_{adh} = \Delta E_{strain} + \Delta E_{int} \tag{5}$$

To analyze the electronic properties, we plot the density of states (DOS), the Crystal Orbital Hamilton Population (COHP)[53], and the chemical bonding analysis[54] using the LOBSTER code[55].

2.3. Structural models

2.3.1. Bulk maghemite

Maghemite comes from oxidation of magnetite (Fe_3O_4) and thus presents a similar spinel structure, apart from substitution of some cations by vacancies to ensure charge neutrality. According to numerous experimental studies, maghemite can keep the cubic space group $P4_332$ (or $P4_132$) [56, 57, 58, 59, 60, 31, 19] or further to a vacancies ordering, often occurring in larger systems, the symmetry can decrease towards tetragonal group $P4_12_12$ [61, 62, 19, 1]. In this paper, we made the choice of keeping the cubic symmetry in consistency with the size of our system, while avoiding a too large unit cell. We thus use a unit cell composed of 8 tetrahedral irons, 13 octahedral irons and 32 oxygens, combined with 3 vacancies at octahedral sites (see SI for structure). This leads to a slightly modified stoichiometry of γ-$Fe_2O_{3.05}$ or $\gamma-(Fe_{Th})_8[(Fe_{Oh})_{13\square_3}O_{32}]$, as already proposed[31]. However, for sake of efficiency, maghemite will be named in the following γ-Fe_2O_3, or simply Fe_2O_3. The computational parameters are optimized with respect to experimental bulk properties such as bandgap, and magnetic properties.[63] The optimized cell parameter (8.39 Å) is in good agreement with experimental data (a = b = c = 8.3565 Å) within 0.5% of error and with a previous theoretical work[31]. We observed a magnetic moment of 2.26 μB/Fe_2O_3, indicating

oppositely aligned spin moments for iron atoms in the cell. This value is in good agreement with an earlier theoretical work (2.28 μB/Fe_2O_3[31]), but deviates from the experimental value obtained for the stoichiometric tetrahedral model (2.5μB/Fe_2O_3[64]). This latter statement can be explained by our excess of Fe-vacancies leading to a small deviation of our cubic model from the standard stoichiometry.

2.3.2. Surface models

To model the (001) surface, a 1×1 supercell cut along the (001) plane is used. We consider a 16-layers slab model, leading to a stoichiometry equivalent to the one of the bulk. Three types of planes can be defined as reported in Figure 1a. Plane A (Fe_{Th}) consists of two tetrahedral iron-atoms; plane B (Fe_{Oh}-O) has eight oxygen atoms and four octahedral iron-atoms; and plane C (Fe_{Oh}-O) is similar to plane B except for a vacancy at an octahedral iron site. When cutting the bulk along (001), as the stoichiometry and number of layers are fixed, the top and bottom surfaces are not identical. We thus obtain four possible combinations of terminations: iron-tetrahedral combined with oxygen/iron-octahedral with and without vacancy named as AB, AC1, AC2, and AC3, according to the labels of the planes previously defined, with additional numbers (1,2,3) to distinguish similar outer layers with different sublayers. In all calculations, ferrimagnetism is respected.
In the case of $\gamma-Fe_2O_3$(111), the bulk surface is cut along (111) plane and the lattice vector is transformed by a C-centre matrix in order to obtain an epitaxial relationship with the Pt(001)-substrate along one direction of the surface. As for the (001) termination, the stoichiometry is kept with an 18-layers slab. This latter is reported on Figure 1b, as well as the following labeling for the different planes: A: eight Fe_{Th}, D: eighteen Fe_{Oh} without vacancy, F: Fe_{Oh} with vacancy, E: thirty-two O atoms sandwitch between Fe_{Oh} and Fe_{Th}. As for the (001), cutting from the bulk leads to two different terminations at each side. Therefore, studied slabs will be a combination of two terminations, leading to four different systems, namely AD1, AD2, EF, and AE.
To study the epitaxial growth of maghemite on Pt(001), the influence of strain, namely the necessary compression applied on maghemite to reach the lattice parameter of platinum, is then considered on both (001) and (111) systems. Finally, all the possible strained terminations are used to build the $\gamma-Fe_2O_3$/Pt(001) composite in order to understand the impact of Pt substrate on the different terminations. A (2×2) supercell of a 5-layers slab

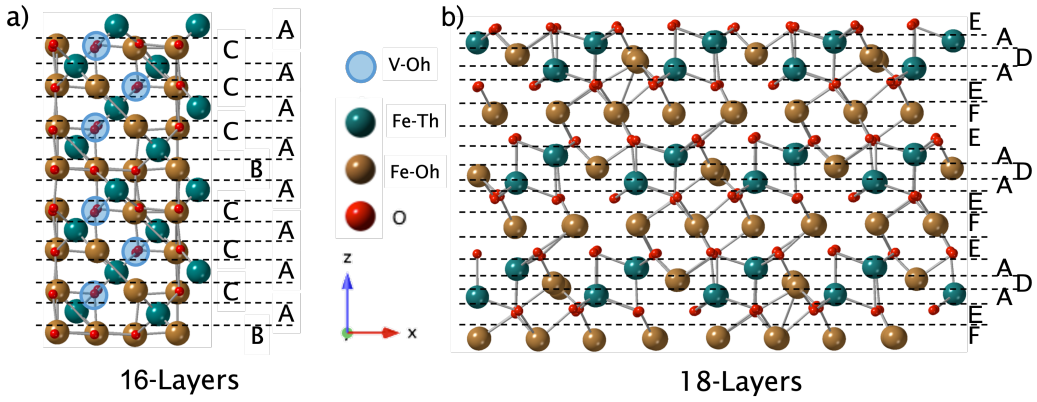

Figure 1: a) 16-layers (001) model of $\gamma-Fe_2O_3$ with planes A (Fe_{Th}), B (Fe_{Oh}-O without octahedral Fe vacancies), and C (Fe_{Oh}-O with octahedral Fe vacancies), b) 18-layers (111) model of $\gamma-Fe_2O_3$ with planes A (Fe_{Th}), E (O layer), D (Fe_{Oh} without vacancy) and F (Fe_{Oh} with vacancy). Oxygen atoms are reported in red, Fe_{Th} in green, Fe_{Oh} in bronze and Fe_{Oh} vacancy in blue.

is used to model the Pt substrate, with $a_{Pt} = 3.92$ Å. The bottom two layers are kept frozen, while top three are allowed to relax. The used unit cells of platinum, for both (001) and (111) maghemite are reported in SI. For each strained maghemite, either (001) or (111), all possible relative positions, such as top, bridge or hollow, with the platinum surface are investigated. Twenty different possibilities for heterostructures are thus considered for the case of (001) and four for the case of (111).

3. Surface structure: $\gamma-Fe_2O_3(001)$ vs. $\gamma-Fe_2O_3(111)$

3.1. Bare surfaces

First step in the understanding of maghemite surfaces involves the study of the different possible terminations of bare surfaces and their relative stability. As mentioned earlier, we have thus investigated four different bare terminations for the 16-layers (001) surface and four for the 18-layers (111) surface. Firstly the cleavage energies are calculated and compared to provide insights on surface stability. A summary of the obtained results is reported in Figure 2.

For the (001) surface, the optimization of the four possible cases mentioned previously leads to four stable systems. The AB slab, namely terminated by Fe_{Th} on one side and Fe_{Oh}-O on the other, is the most stable one

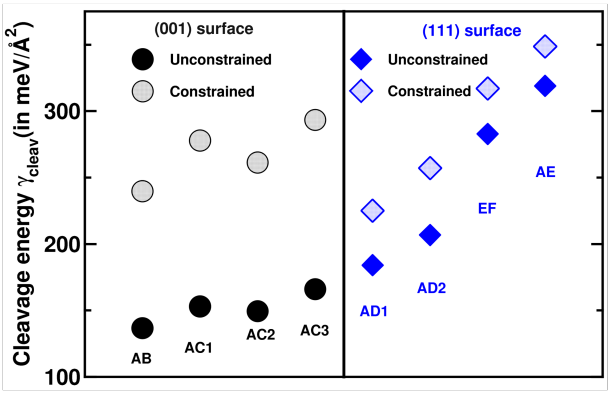

Figure 2: Cleavage energies (in meV/Å^2) calculated according to equation 1 for stable terminations of $\gamma-Fe_2O_3(001)$ and (111) surfaces. Circles and diamonds refer to the (001) and (111) surfaces, respectively, while dark and light shapes refer to native and strained surfaces, respectively.

with a cleavage energy of 136.74 meV/Å^2, followed by AC1 (149.55 meV/Å^2), AC3 (153 meV/Å^2), and AC2 (166.15 meV/Å^2). Slabs with one side presenting an octahedral vacancy are thus always less stable, mainly due to the unsaturated species present on the surface, not compensated by reconstruction. This is in agreement with the recent study of Righi *et al.*[65]. For these three cases (AC1, AC2, AC3), the outer layer is the same (a C plane), only the underneath layers differ. The arrangement of internal layers has thus a non-negligible impact on the relative stability of the different AC-terminations. These results can be positively compared with the previous study of Bentarcurt *et al.*[31], even if they only relax one side of the slab and thus only discuss relative stabilities of top surfaces. Nevertheless, some comparisons can be made. Their most stable termination occurs to be the one with tetrahedral atoms, namely our A layer, present in all our systems, but they also demonstrated that the octahedral layer without vacancy is the second most stable system. This fully agrees with our result of AB, namely a combination of a tetrahedral layer on one side and a complete octahedral layer on the other side, being the most stable case. Besides, they also demonstrated that the presence of subsurface vacancy stabilizes the system. However, in our case, the role of vacancy underneath is destabilizing the system. As AC1 is more stable than AC2 and AC3 despite having Fe_{Oh} vacancy on the underneath layer.

In the case of the (111) surface, after optimization, three combinations

of terminations remain stable: AD (Fe_{Th}-term/Fe_{Oh}-term), with two different cases (AD1 and AD2) depending on the final relaxed surface; AE: (Fe_{Th}-term/O-term); EF: (O-term/Fe_{Oh}-term). Among these possibilities, AD1, namely with iron terminations on both sides is the most stable one (188.08 meV/Å^2), followed by the other combination of iron terminations, AD2 (206.76 meV/Å^2). The last two cases with one side being an oxygen termination are far less stable: EF (284.88 meV/Å^2) and AE (318.70 meV/Å^2), as it was already the case for hematite, with the O_3-termination being widely unfavorable compared to the Fe one.[41] Besides, if we compare the inherent stability, all the (001) terminations are more stable than (111) ones, in agreement with previous results[25].

All these results about stability can now be discussed in terms of geometries. We first analyze the bond lengths of relaxed structures, compared to non-relaxed ones (see Figures 3 and 4). In most cases, the layer underneath is also exposed to the surface. Therefore, reconstruction of those particular layers is expected. During the reconstruction, various bonds are shrunk or elongated, and some new bonds are formed depending on the termination.

There are three classical bonds: $Fe_{Oh}-Fe_{Oh}$ (2.95/3.03 Å), $Fe_{Oh}-O$ (2.01/2.03 Å), and $Fe_{Th}-O$ (1.80/1.89 Å), values in parenthesis refer to the average length of each bond, for (001) and (111) terminations, respectively. However, after optimization, two new $Fe_{Oh}-Fe_{Th}$ ranging from 2.96 to 3.15 Å and $Fe_{Th}-Fe_{Th}$ between 2.65 and 3.10 Å are formed (see Figures 3 and 5). In the case of (001), all structures terminated by Fe_{Th} (A) on one of their sides show a formation of $Fe_{Th}-Fe_{Th}$ bond forcing the surface Fe_{Th} to coordinate with a Fe_{Th} present below the other layers. In particular, these strong $Fe_{Th}-Fe_{Th}$ bonds contribute to the stability of AB and AC terminations. Even the formation of $Fe_{Oh}-Fe_{Th}$ bond comes from the surface reconstruction of layer A. The interactions between the surface and the layer underneath are increased by mixing of the A layer with underneath layer B or C, resulting in a A-B or a A-C facet. Furthermore, one of the Fe_{Th} from A layer occupies the vacancy site of underneath Fe_{Oh} and another one goes into sublayer resulting in formation of a plane with three Fe_{Th} atoms (see Figure:3). In all of the AC cases, the formation of an oxygen molecule occurs on the C side of the surface, and in the case of AC1, the oxygen molecule is even desorbed.

Layer A is present in the initial state of the four studied cases, but after reconstruction, the new facets differ significantly. In AB, AC2, and AC3

cases, the underneath layer of A is C. Therefore, the reconstructed layer, coming from the combination of the top two layers, has the same number of atoms (13) in all three cases. Surprisingly, the same holds true for the AC1 case where the underneath layer is B, so the total number of atoms should be 14 for the reconstructed A-B layer. Here, one of the Fe_{Th} atoms from layer A is pushed below the reconstructed layer, keeping the number of atoms on the reconstructed layer at 13. This is due to the unavailability of vacancy in layer B and thus not all the atoms can be accommodated on the surface. AB, AC2, and AC3 have thus two Fe_{Th} and three Fe_{Oh}, however, AC1 has four Fe_{Oh} and only one Fe_{Th}. No reconstruction takes place on the other side of the surface, that is, B or C. This agrees with results of Bentarcurt *et al.*[31], where large reconstructions were observed for surfaces with tetrahedral irons, while only very limited changes occurred for terminations with octahedral irons. Apart from some relaxation, Fe-O bonds become shorter as compared to the bulk. The perturbation of reconstruction and relaxation remains limited to two or three layers of the surface. Among all the structures, AC1 remains the most planar surface.

The spin density integration around the PAW spheres for octahedral Fe atoms results in local magnetization of 4.13 ± 0.19 μB and for tetrahedral Fe atoms -4.01 ± 0.02 μB. These results are in excellent agreement with those reported earlier[1, 62]. A very small net moment (0.22 μB or less) is observed on the O anions. From bulk to surfaces, a slight decrease in local magnetic moment by about 0.05 μB is noted, mainly due to an increase or decrease in the magnetic moment of the atoms of the surface.

Some of the above observations hold true for the (111) surface, despite additional complexity compared to (001). Formation of new $Fe_{Oh}-Fe_{Th}$ and $Fe_{Th}-Fe_{Th}$ bonds (see Figures 4 and 5) takes place mainly due to surface reconstruction of the Fe_{Th}-layer. As the (111) surfaces are significantly larger than (001), their average bond-lengths remain close to the bulk one, in contrast with the (001) surface. We observed a shorter $Fe_{Oh}-O$ (1.88 vs. 1.91 Å) and a longer $Fe_{Oh}-Fe_{Oh}$ (3.04 vs. 2.95 Å) as compared to the (001) surface. The key difference comes from the Fe_{Th} surface. This surface is heavily reconstructed on the (001) surface, while on the (111) surface the Fe_{Oh} surface with a vacancy is the most affected.

AD1, AD2 and AE all have a Fe_{Th} surface on one side but present different reconstructions, demonstrating again the role of underneath layers. In AD1, some of the oxygens from the underlayer come out of the surface and pull connected Fe atoms upwards from the surface. However, in AD2, oxygen

atoms remain intact on the surface. The perturbation can be noticed on top two layers of Fe_{Th} side. On the other hand, at the other side of the surface (D layer, namely Fe_{Oh} without vacancy), top three layers are disturbed. Fe_{Oh} remains on outermost side while some atoms of the underneath layer of Fe_{Th} go to the oxygen layer, and several oxygen atoms are also pushed upwards. Furthermore, the structural arrangement is not equivalent for AD1 and AD2 surfaces. Fe_{Th} termination side of AD2 surface is more regular than AD1.

On the other hand, for the F-layer (Fe_{Oh} with vacancy), the reconstruction is even more dramatic. Many of Fe_{Oh} atoms penetrate through the surface and go up to three layers. This results in a rugged surface on this side of termination. There are eight Fe_{Oh}, eight Fe_{Th}, thirty-two O and eighteen Fe_{Oh} in that order, which results in eight Fe_{Th}- four Fe_{Oh} and thirty-two O as one layer, and four other Fe_{Oh} are being pushed towards the underneath layer.

AE and EF both involve at least one O-termination on one side. For EF, the oxygen termination (layer E) remains the most stable thanks to Fe_{Th} below the oxygen layer. This combination seems to be more favorable compared to the case of AE. Indeed, octahedral irons below the oxygen termination (layer E) induce significant reconstruction. The oxygen layer forms several vacancy sites, leading to the formation of O_2 and O_3 species interacting with the surface. This is an interesting case where the surface naturally generates vacancies and can facilitate the adsorption of reactive species on the surface. On the other hand, the reconstruction of Fe_{Th} occurs very differently compared to AD1 or AD2. The reconstructed layer is a combination of O, Fe_{Th} and Fe_{Oh}, where some of the oxygens are on the surface and some remain intact on the underlayer. The surface is slightly less irregular than AD1 or AD2.

3.2. Effect of strain

To model the interface of Pt(001) with $\gamma-Fe_2O_3$ surface, we need to consider the strain effect due to the lattice mismatch between Pt(001) and either $\gamma-Fe_2O_3$ (001) or (111). The supercell is constructed in such a way that the lattice mismatch is minimized. For surface (001), the strain is 6.56% along the x and y directions, while for the (111) surface, the strain is 0.86% along the x-direction and 4.64% along the y-one. Due to strain, most of the surfaces are slightly destabilized. However, the impact is not of the same order of magnitude on all systems.

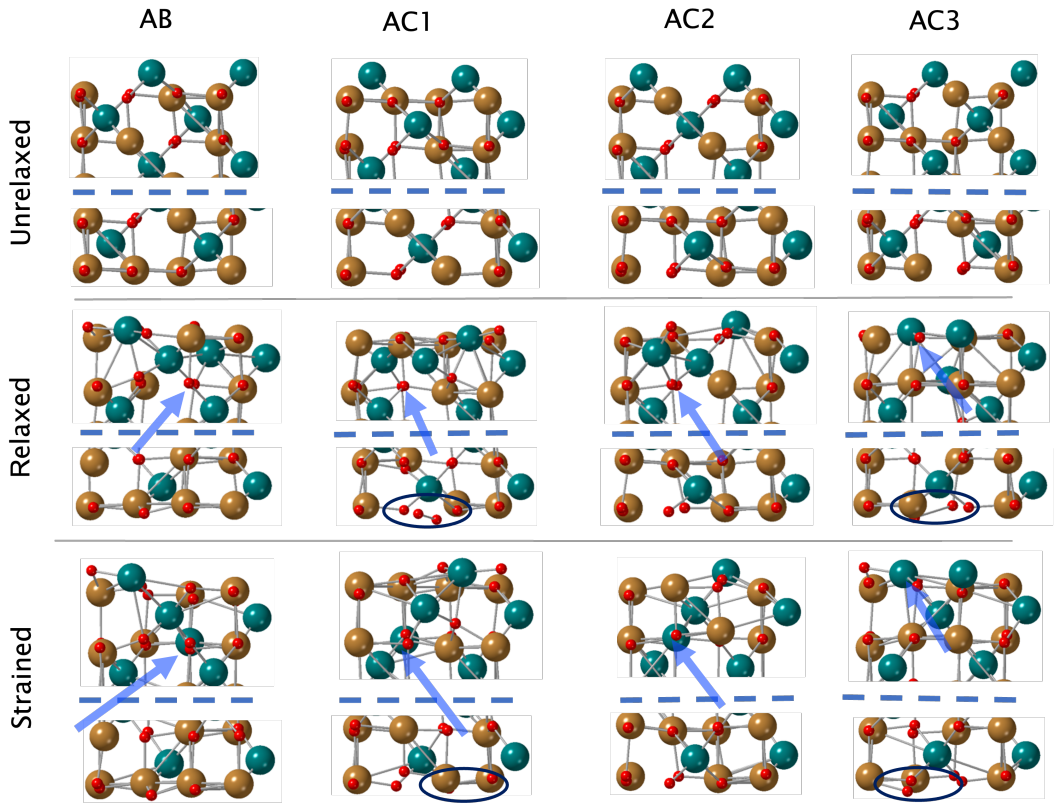

Figure 3: The four possible terminations of $\gamma-Fe_2O_3(001)$: AB, AC1, AC2, AC3 (from left to right). Top panel shows Unrelaxed surfaces (directly cut from the bulk), middle panel reports the same surfaces after relaxation, and the bottom panel shows constrained relaxed surfaces. The dashed blue line represents the missing bulk part of the surface, as here, we only show the top/bottom 4-5 layers for each case. The blue arrows indicate the location of octahedral vacancy (relaxed panel) occupied by Fe-Th atoms when applied strain. The black circle indicates O_2 or O_3 species formation on the surface.

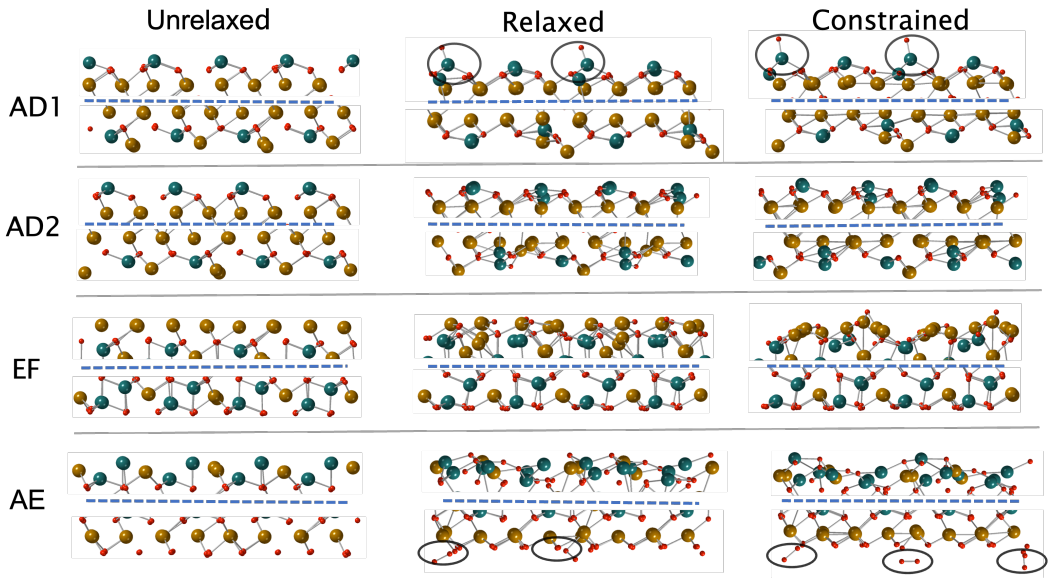

Figure 4: The four possible terminations of $\gamma-Fe_2O_3(111)$: AD1, AD2, EF and AE (from top to bottom). Left panel shows unrelaxed surfaces (directly cut from the bulk), middle panel reports the same surfaces after relaxation, and right panel shows constrained relaxed surfaces. For sake of clarity, the slab centers (not significantly modified under relaxation and strain) are not reported. (See SI for complete structures). Only top and bottom 2-4 layers have been displayed; blue dotted line differentiate the top and bottom layers of the surfaces. The blue circles indicate the formation of O_2 or O_3 species at AE surface and top-O on AD1 surface.

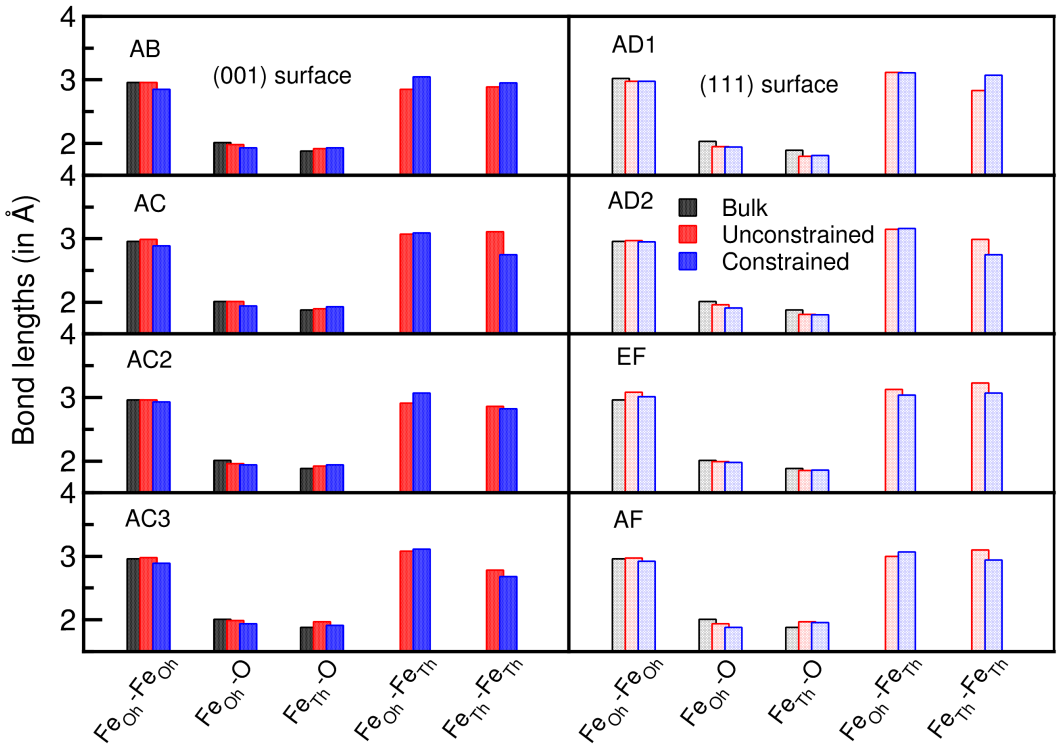

Figure 5: Comparison of various bond lenghts in Å. Average values for bulk are reported in black, while values for unconstrained and constrained relaxed surfaces are reported in red and blue, respectively. (001) and (111) surfaces are reported on left and right panels, respectively.

In the case of (001) terminations, the impact of strain is relatively similar for most cases. All the surfaces are destabilized by the strain significantly. However, the stability order does not evolve due to strain. It is important to mention that even if both sides of the outer layers have the same surface, for example, AC, AC2, and AC3, the impact of strain still differs. Therefore, as for the unconstrained systems, the inner layers play a crucial role in stability.

The strain causes significant changes in the structure of the surface in most cases. The A side of the surface undergoes similar reconstructions for AB, AC1, and AC2. One of the Fe_{Th} atoms from the three-Fe_{Th}-atom layer moves to a deeper sublayer and takes the position of a Fe_{Oh} vacancy. The $Fe_{Oh}-Fe_{Th}$ bonds are elongated for all cases, while the $Fe_{Th}-Fe_{Th}$ bonds shrink for most cases, except AB. In general, the Fe_{Th}-O bond is stretched compared to the Fe_{Oh}-O bond, which is shortened in most cases. The $Fe_{Oh}-Fe_{Oh}$ bonds may be shortened or remain unchanged due to the strain effect which does not disturb the octahedral layers much. Except for AB, O-O (2.5Å) bonds are formed in all cases, but the oxygen molecules remain strongly attached to the system. In the case of AC3, the sublayer is composed of Fe_{Oh} atoms without vacancies, keeping the two Fe_{Th} atoms in the top layer and the rest of the inner part of the system remains similar to the bulk. In all cases, various Fe_{Th} atoms occupy the position of Fe_{Oh} vacancies either on the top layer or the sublayers but do not create Fe_{Th} vacancies.

For (111) surfaces, the strain always destabilizes the different terminations, but without any change in the relative order of stability. Moreover, the impact on the most stable cases is greater than on less stable ones. In particular, the terminations that involve oxygen (EF and AE) are weakly impacted in contrast with terminations with iron atoms on both sides (AD1, AD2). This has already been observed for hematite, for which the O_3-termination is less affected by strain than the Fe-one.[41] The same holds true for the (001) surface, except oxygen termination on (001) also involves iron atoms (layer C, see Figure 2). No significant reconstruction is observed in any of the terminations at the (111) surface, apart from some bonds present at the surface becoming shorter. For EF, as there are many Fe_{Oh} atoms present on the surface due to strain, the surface becomes wavelike (Figure 4). In a similar manner, some of the Fe_{Th} are pushed out of the surface from the AE termination. Among all the (001) and (111) terminations, after the strain effect, AD1 is the most stable followed by AB, AD2, AC2, AC1, and AC3.

Finally, strain has only a slight impact on the local magnetic moment.

The magnetic moment increases by 0.04 μB for AB, AC1, and AC2 with respect to the bulk. However, in case of AC3 it decreases by 0.03 μB. The average local charge on iron atoms is also not affected. Only a minor increase or decrease of about ± 0.15 e^- in charge is observed.

3.3. γ-Fe_2O_3/Pt interface

Finally, we study the heterostructures by combining strained surfaces of maghemite with Pt(001). Three possible sites have to be considered for the relative position of γ-Fe_2O_3 on platinum: top, hollow, and bridge. While considering facets of the surfaces, it generates twenty heterostructures for the (001) surface. However, as calculations for the (111) termination on Pt(001) are computationally very expensive, we consider only the four most stable ones. The initial configurations are named depending on the position of the Fe atom of the Fe-termination towards the Pt(001) surface. Nevertheless, for the (111) surface, the distinction among top, hollow, and bridge is not very clear as some Fe atoms fall on more than one type of site. The energies of the most stable configurations for both terminations are reported in Table 1, while the corresponding structures are reported in Figures 6 and 7. Only the most stable cases are now discussed for both surfaces.

To evaluate the stability of the surfaces, we compute the formation energy, as defined in equation 5. Moreover, to form a stable heterostructure, it is important to overcome the offset induced by the strain. Therefore, we also consider the adhesion energy as the sum of strain energy and interaction energy. It gives an indication of the feasibility of the growth of a given surface on Pt substrate. All energies are calculated per surface unit, to allow a direct comparison between (001) and (111) terminations.

In terms of interaction energy, EF shows the strongest interaction with the Pt surface due to several Pt-O bonds, stabilizing the system. Indeed, the importance of the strength of Pt-O bonds for epitaxial growth has already been evidenced for hematite[41]. Interaction energy helps to overcome the intrinsic instability of oxygen termination and makes it the most favorable case on the Pt substrate. We also calculate the formation energy per surface unit on the Pt substrate with respect to the bulk. According to formation energy, EF (33.01 meV/Å^2) is the most accessible termination that can grow over the Pt(001) substrate, followed by AD2 (48.92 meV/Å^2), AD1 (88.02 meV/Å^2) AC2 (103.37 meV/Å^2), AB (108.90 meV/Å^2), AC1 (116.38 meV/Å^2), and AC3 (133.96 meV/Å^2). Though (001) appears to be more stable as a bare

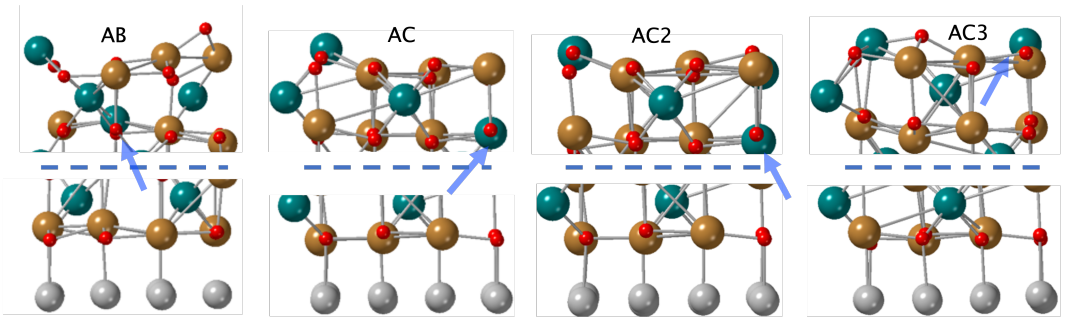

Figure 6: Most stable relaxed heterostructures of $\gamma-Fe_2O_3(001)/Pt(001)$: AB, AC1, AC2, and AC3 terminations, respectively. For the sake of clarity, only the top layer of substrate are displayed. Blue arrow shows the occupied Fe-Oc vacancy site by Fe-Th atom.

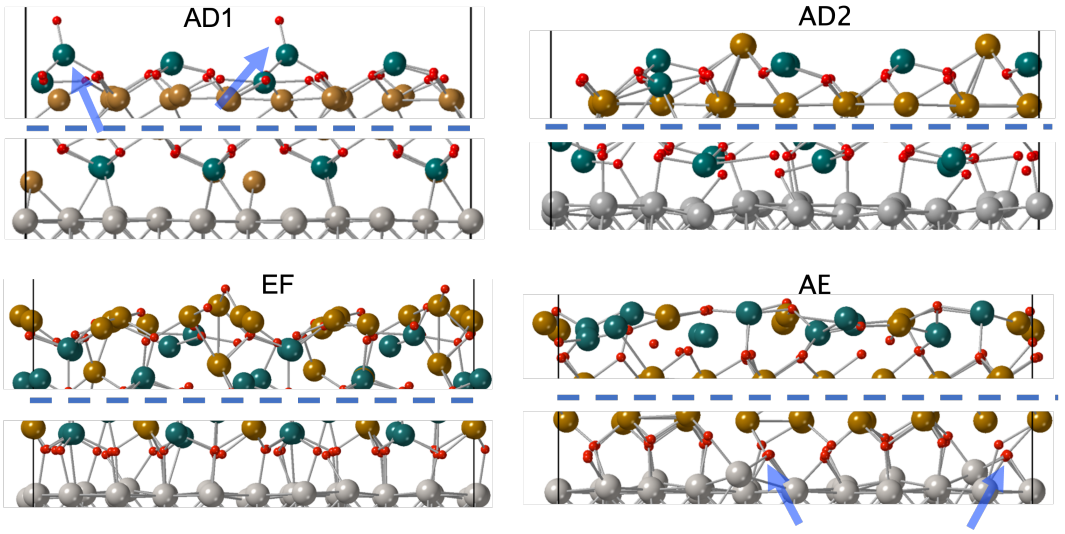

Figure 7: Most stable relaxed heterostructure of $\gamma-Fe_2O_3(111)/Pt(001)$: AD1, AD2, EF, and AE respectively. For the sake of clarity, only the top layer of the substrate are displayed.

surface, on Pt(001) substrate, the (111) termination of maghemite predominantly becomes more stable over (001) with almost half (AD2 vs AB/ACs) or one-third (EF vs AB/ACs) of the required formation energy with respect to (001) surface. This clearly indicates the dominance of (111) surface over (001) on Pt substrate. This observation is also confirmed by adhesion energy.

If we only compare the interaction energy, (111) terminations show more significant interaction than (001). Among them, oxygen layers or layers that contain oxygen atoms predominantly lead to higher interactions. In most cases of (001) surface, the most stable interaction occurs either from the B or C layer but not from the A layer, due to the absence of Pt-O interactions for this layer. Moreover, the respective Fe atoms present on the layer also accommodate themselves in such a way that the number of Pt-O bonds can be maximised. The situation slightly differs in the case of (111), where Fe and O atoms are not simultaneously present in the same layer. Therefore, there is no possibility of maximizing the O bonds. In that case, only Pt-Fe or Pt-O bonds can exist, with the exception of AD2, where underlayer oxygen atoms start interacting with the substrate. In all cases, (001) or (111), Fe (tetrahedral or octahedral) always likes to sit either on the bridging site or on the hollow site of the platinum surface and oxygen atoms on top of a Pt. EF has the highest number of oxygen atoms in the outer layer therefore, can exhibit the highest number of Pt-O bonds and require the lowest formation energy.

Surface termination	1/2*Cleavage energy unconstrained / constrained	Strain energy	Interaction energy	Adhesion energy	Formation energy
AB	68.37 / 119.87	83.10	-130.84	-47.74	108.90
AC1	76.50 / 138.93	102.60	-161.48	-58.88	116.38
AC2	74.77 / 130.63	89.96	-157.90	-67.95	103.37
AC3	83.07 / 142.70	103.09	-159.46	-56.37	133.96
AD1	92.04 / 112.52	30.27	-137.04	-106.77	88.02
AD2	104.95 / 127.86	33.59	-206.77	-173.18	48.92
EF	142.42 / 158.50	15.58	-283.98	-268.40	33.01
AE	160.76 / 174.24	08.27	–	–	–

Table 1: Comparison of cleavage, strain, interaction, adhesion, and formation energies of various (001) and (111) terminations. All values are in meV/Å^2. Corresponding heterostructures are reported in figures 6 and 7.

4. Electronic properties

4.1. Density of states

The projected densities of states (PDOS) for each slab are plotted in Figures 8 and 9. To better highlight the evolution of oxygen and iron states, only iron and oxygen atom densities are displayed, even for Pt-supported systems. The zero of the energy scale is shifted to the respective Fermi energy of the system. Shift in Fermi energy plays a crucial role in the stability of the slab and heterostructure. The common feature in the valence band mainly consists of O-p states while the conduction band is mainly attributed to Fe-d states of Fe_{Th} as spin-up and Fe_{Oh} spin down, near Fermi level. We compare the DOS of the pristine surface with respect to both strain effect and adsorption on Pt(001). In comparison with bulk DOS[31], a small number of states appears in the bandgap region, mostly consisting of O-Fe states, in agreement with earlier observations[31, 35].

The Fermi energy is close to the valence band in all cases except AB where the bandgap is very small due to a small number of states appearing in the bandgap region on bare surfaces. Under constrain the fermi energy is shifted to the middle of the valence band (VB) for most cases except AC1 where the bandgap is reduced due to new states arising between the VB and conduction band (CB) When adsorbed on top of the Pt(001) substrate, the fermi energy is shifted towards the CB in all cases except AB where it shifted towards the VB. Change in the position of Fermi energy indicates the evolution in electronic properties of the surface. The Fermi energy of AB is closer to the valence band than ACs. The shift in Fermi energy toward VB stabilizes the surfaces, and towards CB destabilizes. On Pt substrate, the small number of states that were present in the bandgap region is either reduced or disappeared (Figures 8 and 9) as the unsaturated species present on the surface are reduced with Pt-interaction. For most cases, some of the d-unoccupied states of Fe_{Oh} are transferred to the occupied states due to the Fe-Pt interaction. Changes in oxygen-p states are also observed due to the Pt-O interaction.

For (111) surfaces, Fermi energy does not change its position significantly. A small number of states appears in the bandgap region, as in the case of (001), which diminishes or reduces after adsorption on the Pt substrate. Overall, the pDOS does not evolve much for the (111) case near Fermi energy, in contrast with (001). The evolution is mainly observed on the conduction band spin-up densities of Fe_{Th}-d and spin-down densities of Fe_{Oh}-d of AD2

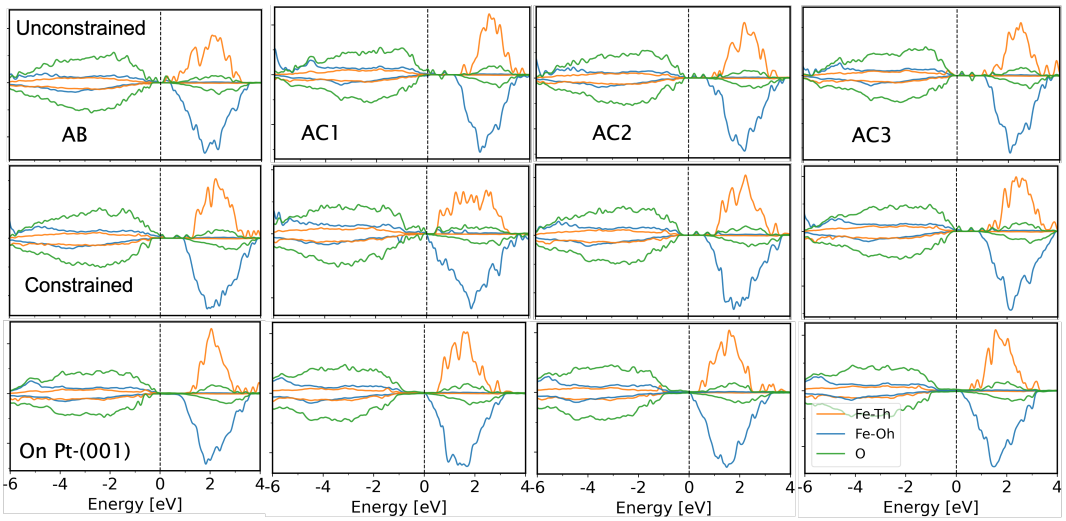

Figure 8: Density of states of various terminations of $\gamma-Fe_2O_3(001)$: unconstrained, constrained, and on Pt substrate. The zero of the energy scale is set to be respective Fermi energy. Only the most stable case is shown for $\gamma-Fe_2O_3$/Pt heterostructure. For simplicity, only iron and oxygen states are reported.

and EF. Oxygen-p states do not evolve except for the EF where an entire layer of oxygen atoms is interacting with the Pt substrate.

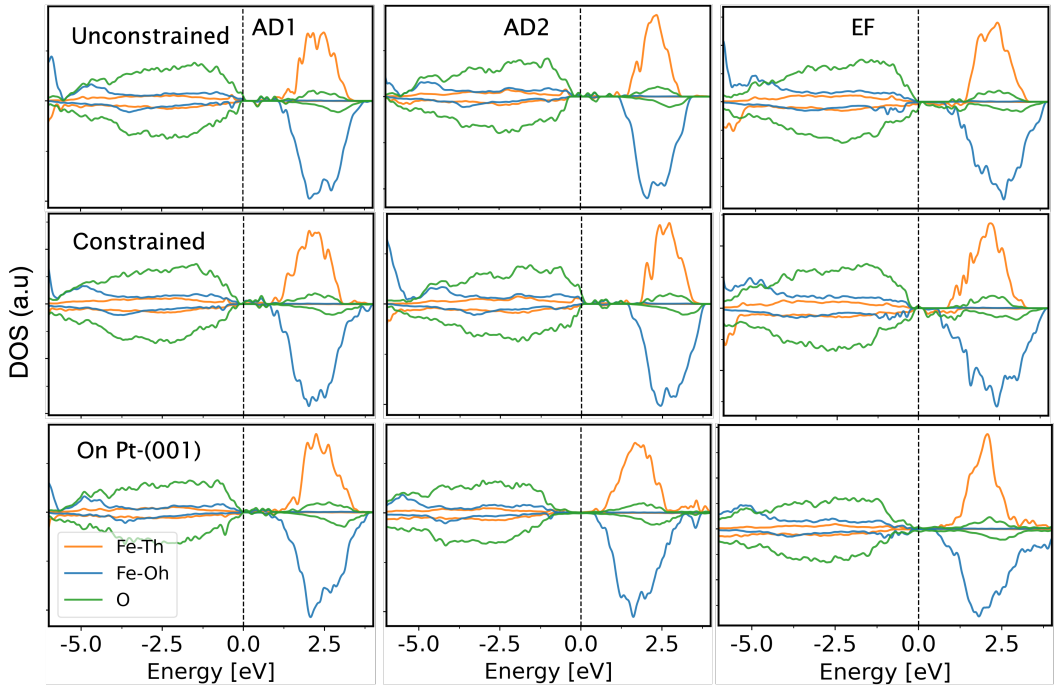

Figure 9: Density of states of various terminations of $\gamma-Fe_2O_3(111)$: unconstrained, constrained, and on Pt substrate. The zero of the energy scale is set to be respective Fermi energy. Only the most stable case is shown for $\gamma-Fe_2O_3$/Pt heterostructure. For simplicity, only iron and oxygen states are reported.

4.2. Crystal Orbital Hamilton Population (COHP) analysis and charge transfer

Finally, to understand the nature of bonding and anti-bonding of (001) surfaces and thus understand the change in the order of stability after applying strain; we plot the crystal orbital Hamilton population (see Figure 10). A higher number of bonding states demonstrates greater stability. The crossing point of bonding and anti-bonding states thus evolves according to stability. In a bare surface scenario, AB has a greater number of bonding states than anti-bonding; consequently, the crossing point is upwards in contrast with AC2, AC1, and AC3. However, the crossing point changes after applying strain. For all cases the crossing point shifts downwards, indicating lower stability under the strain effect.

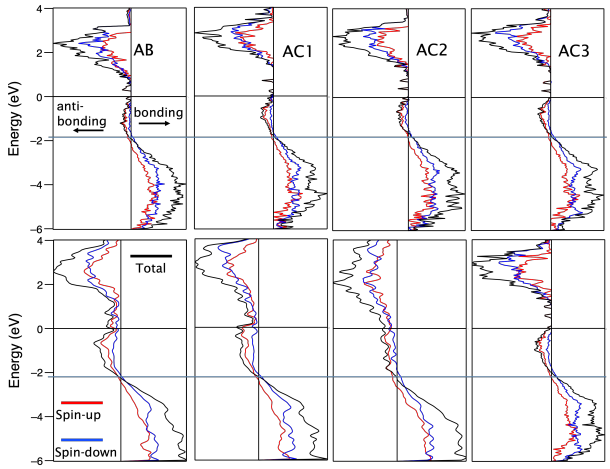

Figure 10: Crystal Orbital Hamilton Population (COHP) for the different terminations of $\gamma-Fe_2O_3(001)$: (Top) unconstrained, and (Bottom) constrained. The zero of the energy scale is set to be the respective Fermi energy. The blue line indicates the crossing point of bonding-antibonding states.

5. Conclusions

A comprehensive study of maghemite surfaces cut along (001) and (111) planes was carried out using the periodic DFT+U method. The surface terminations were studied to characterize their geometry, stability, and electronic properties. The models of the surfaces were constructed from optimized bulk parameters. Cleavage energy was used to describe the stability of the surface, combined with DOS and COHP analysis to analyze the key differences and electronic behavior.

For the (001) termination, a surface with an octahedral vacancy shows lower stability than one without vacancy. Not only the outer layers but also the layers underneath have a significant impact on the surface stability. Under strain, all the surfaces are destabilized. As a consequence, reconstruction takes place and allows to invert some octahedral-tetrahedral Fe. In general, a larger number of Pt-O interactions are preferred on the Pt substrate. AC1 exhibits lower stability on Pt than AC2 despite having the largest interaction energy (among 001 cases) due to several Pt-O interactions because of reconstruction induced by the strain. As a result, the top layer of the epitaxially grown (001)-maghemite surface on Pt(001) substrate would be a combination of A—B layers (Fe_{Th} and Fe_{Oh} without vacancy). Among the different

(111) cases, AD1 is the most stable surface, and here, the strain does not modify the order of stability. No large reconstruction takes place on (111) surfaces due to relaxation/strain. A combination with oxygen termination (EF) is less stable than others but becomes most stable on a Pt substrate due to a large number of Pt-O interactions, which leads to greater stability. Overall, (001) is more stable as a bare surface. However, after incorporating the effect of strain, some of the (111) surfaces become more stable due to the weaker impact of strain and relatively large cell parameters. However, on the Pt substrate, the EF of (111) becomes the most stable one by accumulating huge interaction energy due to several Pt-O bonds. Therefore, as a result, a Fe-octahedral termination can be seen as the most stable surface on Pt(001) from the top view.

Acknowledgments

Calculations were performed using HPC resources from DNUM CCUB (Centre de Calcul de l'Université de Bourgogne). This work was also granted access to the HPC resources of IDRIS under allocations A0110811108 and AD010813498 made by GENCI. The authors also thank the ANR for financial support through project ANR-17-EURE-0002 (EIPHI Graduate School) and OPTYMAL grant ANR-20-CE42-0015-02.

6. Supporting Information

In supporting information we have described the bare Pt-substrate, top-view of (001) surface, and evolution of pair correlation function for various different terminations. Energetic of different explored possibilities of heterostructures have been reported here. Structures of the most stable cases of heterostructures have been also demonstrated. All coordinates of relevant structures have been given in the final section of supporting information.

References

[1] R. Grau-Crespo, A. Y. Al-Baitai, I. Saadoune, N. H. D. Leeuw, Vacancy ordering and electronic structure of γ-Fe_2O_3(maghemite): a theoretical investigation, Journal of Physics: Condensed Matter 22 (25) (2010) 255401. doi:10.1088/0953-8984/22/25/255401.

[2] H. Shokrollahi, A review of the magnetic properties, synthesis methods and applications of maghemite, Journal of Magnetism and Magnetic Materials 426 (2017) 74–81. doi:10.1016/j.jmmm.2016.11.033.

[3] R. V. Jagadeesh, H. Junge, M. Beller, Green synthesis of nitriles using non-noble metal oxides-based nanocatalysts, Nature Communications 5 (1) (2014) 4123. doi:10.1038/ncomms5123.

[4] H. Kuhlenbeck, S. Shaikhutdinov, H. J. Freund, Well-ordered transition metal oxide layers in model catalysis – a series of case studies, Chemical Reviews 113 (6) (2013) 3986–4034. doi:10.1021/cr300312n.

[5] R. V. Jagadeesh, K. Natte, H. Junge, M. Beller, Nitrogen-doped graphene-activated iron-oxide-based nanocatalysts for selective transfer hydrogenation of nitroarenes, ACS Catalysis 5 (3) (2015) 1526–1529. doi:10.1021/cs501916p.

[6] R. V. Jagadeesh, A.-E. Surkus, H. Junge, M.-M. Pohl, J. Radnik, J. Rabeah, H. Huan, V. Schünemann, A. Brückner, M. Beller, Nanoscale Fe_2O_3-based catalysts for selective hydrogenation of nitroarenes to anilines, Science 342 (6162) (2013) 1073–1076. doi:10.1126/science.1242005.

[7] K. Qiu, G. Chai, C. Jiang, M. Ling, J. Tang, Z. Guo, Highly efficient oxygen reduction catalysts by rational synthesis of nanoconfined maghemite in a nitrogen-doped graphene framework, ACS Catalysis 6 (6) (2016) 3558–3568. doi:10.1021/acscatal.6b00531.

[8] M. Skrzypkiewicz, I. Lubarska-Radziejewska, J. Jewulski, The effect of Fe_2O_3 catalyst on direct carbon fuel cell performance, International Journal of Hydrogen Energy 40 (38) (2015) 13090–13098. doi:10.1016/j.ijhydene.2015.07.132.

[9] W. Jiang, M. Pelaez, D. D. Dionysiou, M. H. Entezari, D. Tsoutsou, K. O'Shea, Chromium(VI) removal by maghemite nanoparticles, Chemical Engineering Journal 222 (2013) 527–533. doi:10.1016/j.cej.2013.02.049.

[10] T. Tuutijärvi, J. Lu, M. Sillanpää, G. Chen, As(V) adsorption on maghemite nanoparticles, Journal of Hazardous Materials 166 (2) (2009) 1415–1420. doi:10.1016/j.jhazmat.2008.12.069.

[11] A. Afkhami, R. Norooz-Asl, Removal, preconcentration and determination of Mo(VI) from water and wastewater samples using maghemite nanoparticles, Colloids and Surfaces A: Physicochemical and Engineering Aspects 346 (1) (2009) 52–57. doi:10.1016/j.colsurfa.2009.05.024.

[12] D. Fatemeh, M. Elisabeth, T. Mohammad, S. Jani, J. Hua, G. Bilal, M. Galina, K. Tanja, Catalyst support effect on the activity and durability of magnetic nanoparticles: toward design of advanced electrocatalyst for full water splitting, ACS Applied Materials & Interfaces 10 (37) (2018) 31300–31311. doi:10.1021/acsami.8b08830.

[13] W. L. Kwong, C. C. Lee, A. Shchukarev, E. Björn, J. Messinger, High-performance iron (III) oxide electrocatalyst for water oxidation in strongly acidic media, Journal of Catalysis 365 (2018) 29–35. doi:10.1016/j.jcat.2018.06.018.

[14] M. Tavakkoli, T. Kallio, O. Reynaud, A. G. Nasibulin, J. Sainio, H. Jiang, E. I. Kauppinen, K. Laasonen, Maghemite nanoparticles decorated on carbon nanotubes as efficient electrocatalysts for the oxygen evolution reaction, Journal of Materials Chemistry A 4 (2016) 5216–5222. doi:10.1039/C6TA01472K.

[15] Z. Wang, B. Yang, X. Zhao, Y. Chen, D. Wei, L. Zhang, X. Su, Facile synthesis of ultrathin γ-Fe_2O_3 magnetic nanosheets rich in oxygen vacancies and their photocatalytic activity for water oxidation, Applied Surface Science 578 (2022) 151999. doi:10.1016/j.apsusc.2021.151999.

[16] S. Dey, S. Sun, N. S. Mehta, Carbon monoxide catalytic oxidation over various iron-based nanoparticles at ambient conditions: A review, Carbon Capture Science Technology 1 (2021) 100013. doi:10.1016/j.ccst.2021.100013.

[17] S. Chandrasekaran, S. H. Hur, E. J. Kim, B. Rajagopalan, K. F. Babu, V. Senthilkumar, J. S. Chung, W. M. Choi, Y. S. Kim, Highly-ordered maghemite/reduced graphene oxide nanocomposites for high-performance photoelectrochemical water splitting, Royal Society of Chemistry Advances 5 (2015) 29159–29166. doi:10.1039/C5RA02934A.

[18] T. Tokubuchi, R. I. Arbi, P. Zhenhua, K. Katayama, A. Turak, W. Y. Sohn, Enhanced photoelectrochemical water splitting

efficiency of hematite (α-Fe_2O_3)-based photoelectrode by the introduction of maghemite (γ-Fe_2O_3) nanoparticles, Journal of Photochemistry and Photobiology A: Chemistry 410 (2021) 113179. doi:10.1016/j.jphotochem.2021.113179.

[19] A. N. Shmakov, G. N. Kryukova, S. V. Tsybulya, A. L. Chuvilin, L. P. Solovyeva, Vacancy ordering in γ-Fe_2O_3: Synchrotron x-ray powder diffraction and high-resolution electron microscopy studies, Journal of Applied Crystallography 28 (2) (1995) 141–145. doi:10.1107/S0021889894010113.

[20] M. P. Morales, C. J. Serna, F. Bødker, S. Mørup, Spin canting due to structural disorder in maghemite, Journal of Physics: Condensed Matter 9 (25) (1997) 5461–5467. doi:10.1088/0953-8984/9/25/013.

[21] T. Hiemstra, Surface structure controlling nanoparticle behavior: magnetism of ferrihydrite, magnetite, and maghemite, Environmental Science: Nano 5 (2018) 752–764. doi:10.1039/C7EN01060E.

[22] X. Wei, Z. Wei, L. Zhang, Y. Liu, D. He, Highly water-soluble nanocrystal powders of magnetite and maghemite coated with gluconic acid: Preparation, structure characterization, and surface coordination, Journal of Colloid and Interface Science 354 (1) (2011) 76–81. doi:10.1016/j.jcis.2010.10.049.

[23] H. Wang, L. Zhang, Z. Chen, J. Hu, S. Li, Z. Wang, J. Liu, X. Wang, Semiconductor heterojunction photocatalysts: design, construction, and photocatalytic performances, Chemical Society Reviews. 43 (2014) 5234–5244. doi:10.1039/C4CS00126E.

[24] M. G. Walter, E. L. Warren, J. R. McKone, S. W. Boettcher, Q. Mi, E. A. Santori, N. S. Lewis, Solar water splitting cells, Chemical Reviews 110 (11) (2010) 6446–6473. doi:10.1021/cr1002326.

[25] R. C. Baetzold, H. Yang, Computational study on surface structure and crystal morphology of γ-Fe_2O_3: toward deterministic synthesis of nanocrystals, The Journal of Physical Chemistry B 107 (51) (2003) 14357–14364. doi:10.1021/jp035785k.

[26] T. Belin, N. Millot, F. Villiéras, O. Bertrand, J. P. Bellat, Structural variations as a function of surface adsorption in nanostructured particles, The Journal of Physical Chemistry B 108 (17) (2004) 5333–5340. doi:10.1021/jp0310899.

[27] R. Frison, G. Cernuto, A. Cervellino, O. Zaharko, G. M. Colonna, A. Guagliardi, N. Masciocchi, Magnetite–maghemite nanoparticles in the 5–15 nm range: Correlating the core–shell composition and the surface structure to the magnetic properties. a total scattering study., Chemistry of Materials 25 (23) (2013) 4820–4827. doi:10.1021/cm403360f.

[28] S. Chambers, S. Joyce, Surface termination, composition and reconstruction of $Fe_3O_4(001)$ and γ-$Fe_2O_3(001)$, Surface Science 420 (2) (1999) 111–122. doi:10.1016/S0039-6028(98)00657-8.

[29] Y. Gao, Y. J. Kim, S. A. Chambers, Preparation and characterization of epitaxial iron oxide films, Journal of Materials Research 13 (7) (1998) 2003–2014. doi:10.1557/JMR.1998.0281.

[30] F. C. Voogt, T. Fujii, P. J. M. Smulders, L. Niesen, M. A. James, T. Hibma, No_2-assisted molecular-beam epitaxy of Fe_3O_4, Fe_3-δO_4, and $\gamma-Fe_2O_3$ thin films on MgO(100), Physical Review B 60 (1999) 11193–11206. doi:10.1103/PhysRevB.60.11193.

[31] Y. L. Bentarcurt, M. Calatayud, J. Klapp, F. Ruette, Periodic density functional theory study of maghemite (001) surface. structure and electronic properties, Surface Science 677 (2018) 239–253. doi:10.1016/j.susc.2018.06.005.

[32] O. Iglesias, A. Labarta, Finite-size and surface effects in maghemite nanoparticles: Monte carlo simulations, Physical Review B 63 (2001) 184416. doi:10.1103/PhysRevB.63.184416.

[33] X. Mou, B. Zhang, Y. Li, L. Yao, X. Wei, D. S. Su, W. Shen, Rod-shaped Fe_2O_3 as an efficient catalyst for the selective reduction of nitrogen oxide by ammonia, Angewandte Chemie International Edition 51 (12) (2012) 2989–2993. doi:10.1002/anie.201107113.

[34] M. Bowker, G. Hutchings, P. R. Davies, D. Edwards, R. Davies, S. Shaikhutdinov, H.-J. Freund, Surface structure of γ-Fe_2O_3(111), Surface Science 606 (21) (2012) 1594–1599. doi:10.1016/j.susc.2012.06.010.

[35] W. Jian, S.-P. Wang, H.-X. Zhang, F.-Q. Bai, Disentangling the role of oxygen vacancies on the surface of Fe_3O_4 and γ-Fe_2O_3, Inorganic Chemistry Frontiers 6 (2019) 2660–2666. doi:10.1039/C9QI00351G.

[36] L. Mazeina, A. Navrotsky, Enthalpy of water adsorption and surface enthalpy of goethite (α-FeOOH) and hematite (α-Fe_2O_3), Chemistry of Materials 19 (4) (2007) 825–833. doi:10.1021/cm0623817.

[37] A. Barbier, A. Stierle, N. Kasper, M.-J. Guittet, J. Jupille, Surface termination of hematite at environmental oxygen pressures: Experimental surface phase diagram, Physical Review B 75 (2007) 233406. doi:10.1103/PhysRevB.75.233406.

[38] G. Ketteler, W. Weiss, W. Ranke, Surface structures of α-Fe_2O_3(0001) phases determined by LEED crystallography, Surface Review and Letters 08 (06) (2001) 661–683. doi:10.1142/S0218625X01001610.

[39] A. Rohrbach, J. Hafner, G. Kresse, Ab initio study of the (0001) surfaces of hematite and chromia: Influence of strong electronic correlations, Physical Review B 70 (2004) 125426. doi:10.1103/PhysRevB.70.125426.

[40] P. Liao, J. A. Keith, E. A. Carter, Water oxidation on pure and doped hematite (0001) surfaces: Prediction of Co and Ni as effective dopants for electrocatalysis, Journal of the American Chemical Society 134 (32) (2012) 13296–13309. doi:10.1021/ja301567f.

[41] A. Mahmoud, P.-M. Deleuze, C. Dupont, The nature of the Pt(111)/α-Fe_2O_3(0001) interfaces revealed by DFT calculations, The Journal of Chemical Physics 148 (20) (2018) 204701. doi:10.1063/1.5033366.

[42] U. Baig, M. Gondal, M. Dastageer, M. Sajid, Maghemite nanoparticles decorated semiconducting graphitic carbon nitride heterostructured nanocomposite: Facile synthesis, characterizations and its visible light active photocatalytic system for removal of hazardous organic pollutants from aqueous solutions, Colloids and Surfaces A: Physicochemical and Engineering Aspects 641 (2022) 128427. doi:10.1016/j.colsurfa.2022.128427.

[43] N. Ferroudj, J. Nzimoto, A. Davidson, D. Talbot, E. Briot, V. Dupuis, A. Bée, M. S. Medjram, S. Abramson, Maghemite nanoparticles and maghemite/silica nanocomposite microspheres as magnetic Fenton catalysts for the removal of water pollutants, Applied Catalysis B: Environmental 136-137 (2013) 9–18. doi:10.1016/j.apcatb.2013.01.046.

[44] M. Tavakkoli, T. Kallio, O. Reynaud, A. G. Nasibulin, J. Sainio, H. Jiang, E. I. Kauppinen, K. Laasonen, Maghemite nanoparticles decorated on carbon nanotubes as efficient electrocatalysts for the oxygen evolution reaction, Journal of Materials Chemistry A 4 (14) (2016) 5216–5222. doi:10.1039/C6TA01472K.

[45] G. Kresse, J. Furthmüller, Efficiency of ab-initio total energy calculations for metals and semiconductors using a plane-wave basis set, Computational Materials Science 6 (1) (1996) 15–50. doi:10.1016/0927-0256(96)00008-0.

[46] G. Kresse, J. Furthmüller, Efficient iterative schemes for *ab initio* total-energy calculations using a plane-wave basis set, Physical Review B 54 (16). doi:10.1103/PhysRevB.54.11169.

[47] G. Kresse, D. Joubert, From ultrasoft pseudopotentials to the projector augmented-wave method, Physical Review B 59 (3) (1999) 1758–1775. doi:10.1103/PhysRevB.59.1758.

[48] J. P. Perdew, K. Burke, M. Ernzerhof, Generalized gradient approximation made simple, Physical Review Letters 77 (1996) 3865–3868. doi:10.1103/PhysRevLett.77.3865.

[49] S. Grimme, J. Antony, S. Ehrlich, H. Krieg, A consistent and accurate ab initio parametrization of density functional dispersion correction (DFT-D) for the 94 elements H-Pu, The Journal of Chemical Physics 132 (15) (2010) 154104. doi:10.1063/1.3382344.

[50] S. L. Dudarev, G. A. Botton, S. Y. Savrasov, C. J. Humphreys, A. P. Sutton, Electron-energy-loss spectra and the structural stability of nickel oxide: An LSDA+U study, Physical Review B 57 (1998) 1505–1509. doi:10.1103/PhysRevB.57.1505.

[51] Y. Meng, X.-W. Liu, C.-F. Huo, W.-P. Guo, D.-B. Cao, Q. Peng, A. Dearden, X. Gonze, Y. Yang, J. Wang, H. Jiao, Y. Li, X.-D. Wen,

When Density Functional Approximations Meet Iron Oxides, Journal of Chemical Theory and Computation 12 (10) (2016) 5132–5144. doi:10.1021/acs.jctc.6b00640.

[52] G. Rollmann, P. Entel, A. Rohrbach, J. Hafner, High-pressure characteristics of α-Fe_2O_3 using DFT+U, Phase Transitions 78 (1-3) (2005) 251–258. doi:10.1080/01411590412331316546.

[53] R. Dronskowski, P. E. Bloechl, Crystal orbital hamilton populations (COHP): energy-resolved visualization of chemical bonding in solids based on density-functional calculations, The Journal of Physical Chemistry 97 (33) (1993) 8617–8624. doi:10.1021/j100135a014.

[54] S. Maintz, V. L. Deringer, A. L. Tchougréeff, R. Dronskowski, Analytic projection from plane-wave and PAW wavefunctions and application to chemical-bonding analysis in solids, Journal of Computational Chemistry 34 (29) (2013) 2557–2567. doi:10.1002/jcc.23424.

[55] R. Nelson, C. Ertural, J. George, V. L. Deringer, G. Hautier, R. Dronskowski, LOBSTER: Local orbital projections, atomic charges, and chemical-bonding analysis from projector-augmented-wave-based density-functional theory, Journal of Computational Chemistry 41 (21) (2020) 1931–1940. doi:10.1002/jcc.26353.

[56] P. Braun, A superstructure in spinels, Nature 170 (1952) 1123. doi:10.1038/1701123a0.

[57] T. Sharifi, E. Gracia-Espino, H. Barzegar, X. Jia, F. Nitze, G. Hu, P. Nordblad, C.-W. Tai, T. Wagberg, Formation of nitrogen-doped graphene nanoscrolls by adsorption of magnetic γ-Fe_2O_3 nanoparticles, Nature Communications 4 (2013) 2319. doi:10.1038/ncomms3319.

[58] I. Chernyshova, M. Hochella Jr, A. Madden, Size-dependent structural transformations of hematite nanoparticles. 1. phase transition, Physical Chemistry Chemical Physics 9 (2007) 1736. doi:10.1039/B618790K.

[59] F. Jiao, J.-C. Jumas, M. Womes, A. Chadwick, H. A., P. Bruce, Synthesis of ordered mesoporous Fe_3O_4 and γ-Fe_2O_3 with crystalline walls using post-template reduction/oxidation, Journal of the American Chemical Society 128 (2006) 12905. doi:10.1021/ja063662i.

[60] W. Wu, X. Xiao, S. Zhang, T. Peng, J. Zhou, R. F., C. Jiang, Synthesis and magnetic properties of maghemite (γ-Fe_2O_3) short-nanotubes, Nanoscale Research Letters 5 (2010) 1474. doi:10.1007/s11671-010-9664-4.

[61] G. van Oosterhout, C. Rooijmans, A new superstructure in gamma-ferric oxide, Nature 181 (1958) 44. doi:10.1038/181044A0.

[62] C. Greaves, A powder neutron diffraction investigation of vacancy ordering and covalence in γ-Fe_2O_3, Journal of Solid State Chemistry 49 (3) (1983) 325–333. doi:10.1016/S0022-4596(83)80010-3.

[63] J. A. R. Guivar, A. I. Martínez, A. O. Anaya, L. D. L. S. Valladares, L. L. Félix, A. B. Dominguez, Structural and Magnetic Properties of Monophasic Maghemite(γ-Fe_2O_3) Nanocrystalline Powder, Advances in Nanoparticles 03 (03) (2014) 114–121. doi:10.4236/anp.2014.33016.

[64] R. Dronskowski, The little maghemite story: A classic functional material, Advanced Functional Materials 11 (1) (2001) 27–29. doi:10.1002/1616-3028(200102)11:1¡27::AID-ADFM27¿3.0.CO;2-X.

[65] G. Righi, R. Magri, Reduction and oxidation of maghemite (001) surfaces: The role of iron vacancies, The Journal of Physical Chemistry C 123 (25) (2019) 15648–15658. doi:10.1021/acs.jpcc.9b03657.